

<https://doi.org/10.1038/s41699-024-00468-7>

Tunable magnetic confinement effect in a magnetic superlattice of graphene

Onur Tosun¹ ✉, Preetha Sarkar¹, Chang Qian², Matthew Gilbert³, Qian Chen² & Nadya Mason⁴ ✉

Two-dimensional van der Waals materials such as graphene present an opportunity for band structure engineering using custom superlattice potentials. In this study, we demonstrate how self-assemblies of magnetic iron-oxide (Fe_3O_4) nanospheres stacked on monolayer graphene generate a proximity-induced magnetic superlattice in graphene and modify its band structure. Interactions between the nanospheres and the graphene layer generate superlattice Dirac points in addition to a gapped energy spectrum near the K and K' valleys, resulting in magnetic confinement of quasiparticles around the nanospheres. This is evidenced by gate-dependent resistance oscillations, observed in our low temperature transport measurements, and confirmed by self-consistent tight binding calculations. Furthermore, we show that an external magnetic field can tune the magnetic superlattice potential created by the nanospheres, and thus the transport characteristics of the system. This technique for magnetic-field-tuned band structure engineering using magnetic nanostructures can be extended to a broader class of 2D van der Waals and topological materials.

Two-dimensional (2D) van der Waals materials such as graphene and transition metal dichalcogenides have unique electronic and optical properties that make them excellent platforms for exploring fundamental phenomena and next-generation devices^{1,2}. Particularly in graphene, with its 2D nature and linear dispersion characteristics, artificial band structure modifications have led to various interesting phenomena which are absent in the pristine materials, such as unconventional superconductivity³, ferromagnetism⁴, and emergence of superlattice Dirac points^{5,6}.

One route to band structure modification is via periodic electrostatic and magnetic structures, which generate periodic potentials^{7–9}. In graphene, it has been theoretically predicted that lattices of Kronig-Penny-type electrostatic potentials can create interesting physical phenomena such as the emergence of finite-energy Dirac points^{10–12} and anisotropic renormalization of group velocity of charge carriers^{13,14}. However, controlling the behavior of the Dirac electrons in graphene using electrostatic potentials is difficult because Klein tunneling prevents electronic confinement¹⁵. On the other hand, it is possible for magnetic potentials, particularly nonuniform magnetic profiles, to confine Dirac electrons in graphene^{16,17}. The electronic band structure of graphene with one-dimensional periodic magnetic barriers has been theoretically predicted to exhibit emergent physical phenomena such as miniband formation and superlattice Dirac points^{13,18,19}. Integration of magnetic nanostructures with graphene thus provides a pathway for generating magnetic superlattice; however, experimental

realization of such systems and study of their electronic properties remains limited.

The current techniques of generating artificial superlattices in graphene, such as Moiré engineering, lithographic patterning, and deposition of adatoms, pose several challenges in terms of reproducibility, scalability, and manufacturing costs. Generating superlattice potentials using lithography is costly and technologically challenging because of the nanoscale resolution required during patterning such potentials. Moiré superlattices of magic angle twisted bilayer graphene^{3,20} and graphene/hexagonal boron nitride heterostructures^{21–23} show remarkable physical phenomena such as superconductivity and fractional Chern insulator behavior. However, in these systems, control over the superlattice periodicity and the effective potential strength is limited. Discovery of 2D magnetic vdW crystals^{24–26} has opened up the possibility of designing heterostructures where interfacial interactions between the 2D magnet and the adjacent non-magnetic layer lead to engineered electronic properties. Apart from inducing magnetism, these interactions can also lead to electrostatic phenomena such as electric-field induced band gap opening²⁷ or large charge doping²⁸. However, to generate a superlattice effect, the magnetic interaction needs to have a periodic modulation. Adsorption of adatoms and clusters on graphene can also modify the band structure^{29,30} and induce behaviors such as magnetism^{31,32} and superconductivity³³, but nanoscale control over the distribution density and periodicity is a challenge. Nanoparticle

¹Department of Physics and Materials Research Laboratory, University of Illinois, Urbana, IL, USA. ²Department of Materials Science and Engineering, University of Illinois, Urbana, IL, USA. ³Department of Electrical and Computer Engineering, University of Illinois, Urbana, IL, USA. ⁴Pritzker School of Molecular Engineering, University of Chicago, Chicago, IL, USA. ✉ e-mail: onurtosunn@gmail.com; nmason1@uchicago.edu

self-assemblies can be a good alternative for overcoming a lot of these challenges especially in terms of maintaining long-range periodicity and reducing production costs. A graphene/iron-oxide (Fe_3O_4) nanospheres (NS) self-assembly system³⁴ showed evidence of proximity induced magnetism, but superlattice effects weren't studied in this system.

In this study, we demonstrate that self-assembled Fe_3O_4 NS arrays generate magnetic superlattice potentials in graphene and modify its band structure. Below the blocking temperature of 50 K, the Fe_3O_4 NS are ferromagnetic and generate proximity-induced magnetism in the underlying graphene. The imprinted magnetism leads to the formation of superlattice Dirac points, even in the absence of an external magnetic field. Further confirmation of the presence of superlattice Dirac points comes from band structure calculations using a self-consistent tight binding model. Measurements of the temperature-dependence of the longitudinal resistance indicate that the charge carriers form closed loop trajectories around the magnetic NS. This magnetic confinement of the charges is evidenced by both the transport data, in the form of quasi-periodic magnetoresistance oscillations, and tight-binding calculations that demonstrate a gapped energy spectrum near the Dirac point. We find that the transport characteristics are the result of an interplay between the magnetization induced by the NS and the effects of an external field, where the external magnetic field can be used to further tune the properties of the magnetic superlattice. This is an experimental demonstration of a magnetic superlattice generated in graphene by proximity-induced magnetism from an array of magnetic nanoparticles and should impact designs of custom superlattice potentials in 2D materials.

Results and discussion

Device fabrication and magnetic characterization

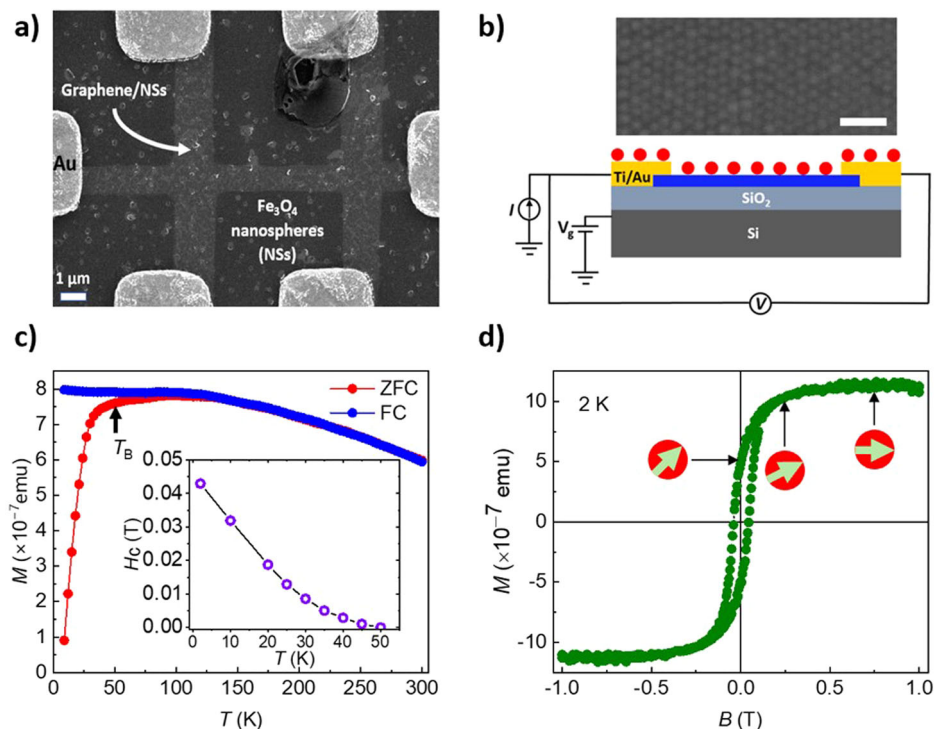
Fe_3O_4 , with its high structural stability and high ferromagnetic ordering temperature^{35,36}, has been chosen to be the core material of the nanoparticles in this study. Fe_3O_4 nanoparticles may be room temperature ferromagnetic^{37,38} or superparamagnetic depending on their size³⁶. In this work, high-quality Fe_3O_4 NS with an average diameter of 10.7 ± 0.7 nm, were synthesized through thermal decomposition of iron oleate³⁵. During synthesis, the iron cores of the NS are surrounded by 1 nm thick oleic acid

shells, which are needed to separate the NS from each other (see Supplementary Note 1 for the experimental details). Monodispersity is a key requirement for nanoparticle building blocks to assemble into large-area and high-precision periodic arrays, and therefore for investigating magnetic structures on graphene^{39–42}. The NSs are spun, and they form puddles only in selected regions, they are not deposited locally on desired regions. The NS were packed into hexagonal monolayer films that have continuous areas of at least tens of micrometers over CVD (chemical vapor deposition) grown monolayer graphene (see Supplementary Note 2 for the experimental details). In this work, exfoliated graphene could be used for better quality and charge carrier mobility. However, it is hard to ensure that monolayer NS assemblies form on top of small, exfoliated pieces. The scanning electron microscopy (SEM) image in Fig. 1a shows hexagonal close-packed monolayer nanoparticles transferred onto a graphene/Si/SiO₂ substrate (see Supplementary Fig. 1 in Supplementary Note 2 for the microscope images confirming the quality of the monodispersed NS). The Fe_3O_4 NS were thermally annealed under forming gas at 300 °C for 30 min to remove the organic ligand shell around the NS for magnetic and electrical characterizations.

Magnetic properties of the annealed Fe_3O_4 NS deposited on SiO₂/Si substrates were studied using a SQUID magnetometer (Quantum Design MPMS3) at temperatures ranging from 300 K to 2 K. The NS were determined to be superparamagnetic with a blocking temperature (T_B) of ~50 K, indicated with an arrow in the zero-field cooled curve at 50 mT shown in Fig. 1c. The T_B was determined by the temperature at which the coercive field is vanishingly small (see inset of Fig. 1c). Below T_B , the NS exhibit ferromagnetic behavior with a clear hysteresis loop, as shown in the magnetization vs. magnetic field curves in Fig. 1d.

Figure 1b shows an illustration of the graphene magnetic superlattice device which consists of magnetic Fe_3O_4 NS, graphene, Ti (5 nm)/Au (20 nm) electrodes, and dielectric SiO₂ (300 nm) on Si, which serves as the back gate. Standard electron beam lithography and reactive ion etching using O₂ plasma were performed to etch the graphene into Hall bar configuration. The electrical transport measurements described in this work were performed on a graphene/ Fe_3O_4 NS device with dimensions of length of $L = 6 \mu\text{m}$ and width of $W = 1 \mu\text{m}$ in a physical property measurement system (Quantum

Fig. 1 | Graphene/NS device and the magnetic properties of Fe_3O_4 nanospheres (NS). **a** Scanning electron microscopy (SEM) micrograph of the backgated graphene magnetic superlattice device. **b** Top is the high-resolution SEM image of the NS. The scale bar represents 50 nm. Bottom is the schematic of the device, with graphene in blue and magnetic NS in red. **c** Zero-field cooled (ZFC) and field-cooled (FC) magnetization curves at 50 mT as a function of temperature showing that the NS are superparamagnetic with a blocking temperature $T_B \sim 50$ K indicated by an arrow. Inset shows coercivity as a function of temperature. The temperature at which the coercive field vanishes is determined to be $T_B = 50$ K. **d** The ZFC magnetization as a function of in-plane magnetic field B at 2 K, showing that the NS are ferromagnetic at 2 K with magnetization orientation pointed out of the plane with an angle. Inset figures show the rotation of the NS magnetization vector with the magnetic field applied at 0 T, 0.25 T, and 0.75 T.



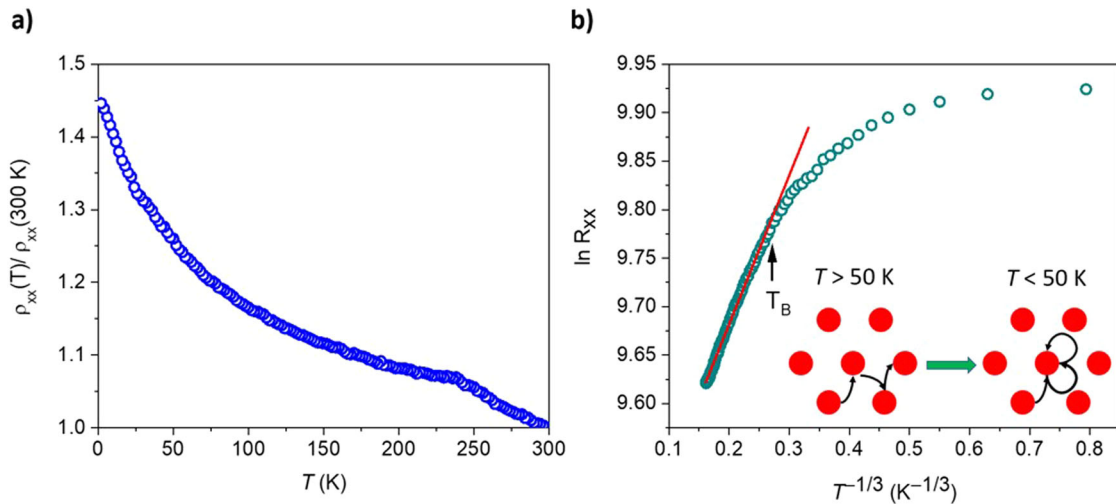


Fig. 2 | Temperature dependence of resistivity and variable range hopping (VRH) in the graphene/Fe₃O₄ nanospheres (NS) system. a Normalized longitudinal resistivity $\rho_{xx}(T)/\rho_{xx}(300\text{ K})$ as a function of temperature. The strong increase in $\rho_{xx}(T)$ with decreasing temperature is an indication of non-metallic behavior. **b** Two-dimensional (2D) VRH fitting ($\ln R_{xx}$ versus $T^{-1/3}$) of $\rho_{xx}(T)/\rho_{xx}(300\text{ K})$ shown in (a). The arrow points to the temperature at which the curve deviates from a

linear relationship for $\ln R_{xx}$ versus $T^{-1/3}$, which is around T_B of the NS. The red line shows the linear fitting for 2D VRH. The inset shows a schematic of a possible 2D hopping mechanism for the charge carriers above and below T_B . The red dots represent the NS with temperature dependent effective magnetic potential profiles. The NS act as scattering centers for the charge carriers and the black arrows represent the hopping trajectory of the charge carriers.

Design PPMS) and using a lock-in amplifier (Model SR830) and a source meter (Keithley 2400) (see the Supplementary Note 3 for details).

Variable-range hopping and magnetic confinement effect

The interaction between graphene and the NS is expected to strongly affect transport properties, especially when considering the ferromagnetic behavior exhibited by the NS below 50 K. The periodic array of Fe₃O₄ nanospheres generates a superlattice potential in graphene via magnetic interactions, with each NS site acting as an extremum for this potential. Incorporating this Kronig-Penny type potential into the Dirac equation results in a band structure with superlattice Dirac points and minibands which are then observed in the transport characteristics. Normalized resistivity $\rho_{xx}(T)/\rho_{xx}(300\text{ K})$ of the graphene magnetic-magnetic NS system, shown in Fig. 2a, indicates an increase in resistivity as the temperature is lowered. The origin of this increase can be understood by considering the transport characteristics of charge carriers in a sample of dense scattering points/localized magnetic moments, as in our device, which may be described by the 2D variable-range hopping (VRH) mechanism. 2D VRH is often observed in thin films or low-dimensional materials where the charge carrier motion is confined to a plane or a narrow region⁴³. The charge transport in the VRH regime is characterized by hopping between localized states. The hopping process occurs due to disorder-induced localization, where impurities or defects create localized energy states within the material's band gap. These localized states act as “islands” where electrons can temporarily reside before hopping to neighboring states⁴³. The resistivity in 2D VRH follows a power law dependence on temperature, given by the expression $\rho \propto \exp(T_0/T)^\alpha$ where T is the temperature, T_0 is the characteristic temperature, and $\alpha = 1/3$ is the power law exponent^{44–46}.

Figure 2b shows the logarithm of the normalized resistance as a function of $T^{-1/3}$ which has a clear linear dependence of $T^{-1/3}$ between 240 K and 50 K indicating that the transport is dominated by quasiparticles hopping between scattering/impurity centers, i.e., the NS with randomly aligned magnetic moments. The kink in the $\rho_{xx}(T)$ around 240 K is an artifact of the measurement system and does not affect the lower temperature data. Below $T_B = 50$ K, the $\ln R_{xx}$ versus $T^{-1/3}$ clearly deviates from the linear relationship for $\alpha = 1/3$. We attribute the deviation to the NS becoming ferromagnetic with their magnetization orientation pointed out of the plane with an angle of transport below T_B . Given the magnetic field profile, the charge carriers are likely confined, and the resulting resistivity is

dominated by closed orbital trajectories around the field lines of the dipole-like magnetic NS⁴⁷. The confinement of the charge carriers then leads to an increase in resistivity upon cooling as shown in Fig. 2a. The inset of Fig. 2b shows a possible mechanism for hopping of the charge carriers above and below T_B . An increase in graphene's resistivity due to strong electron localization has previously been shown in nanostructured graphene antidot systems⁴⁵. Our data is consistent with magnetic NS forming proximity-induced and radially inhomogeneous magnetized regions on graphene. Similar to the antidot system, these magnetized regions likely act as antidots in graphene about which the charge carriers are localized.

Gate-tuning the electrical properties of graphene demonstrates the effects of periodic magnetism on its electronic band structure. The charge carrier density (n) in graphene is tuned by changing back gate voltage (V_g) and determined by using the capacitance⁵ model $n = (C_{ox}/q)(V_g - V_D)$ where $C_{ox} = 1.15 \times 10^{-4} \text{ Fm}^{-2}$ is the capacitance of the 300 nm oxide layer⁴⁸, q is the electric charge, V_D is the voltage at the Dirac point (DP), or, similarly, the charge neutrality point (CNP). The mobility of the device at $V_g = 0\text{ V}$ ($n = 3.6 \times 10^{12} \text{ cm}^{-2}$) is determined to be $\mu = 1155 \text{ cm}^2 \text{ V}^{-1} \text{ s}^{-1}$ using the equation, $\mu = 1/en\rho_{xx} = \frac{L}{enR_{xx}W}$, where ρ_{xx} is the longitudinal resistivity⁴⁸. The corresponding mean free path $l_{mfp} = \frac{\hbar}{e}\sqrt{\pi n}\mu = 26 \text{ nm}$ and the phase coherence length ($L_\phi = 91 \text{ nm}$, which will be discussed later in the text), are larger than the period of the magnetic NS, ensuring the hybrid graphene magnetic NS structure exhibits superlattice behavior.

Figure 3a shows ρ_{xx} vs V_g above and below the magnetic transition temperature. The location of the primary Dirac point V_D at 300 K is determined to be 74 V, while at 2 K it is 50.2 V. Such a shift in V_D may be due to an effective magnetic exchange field imprinted in graphene, as has been theoretically proposed previously⁴⁹. Figure 3a shows that the resistivity at the V_D is increased by a factor of 2 upon cooling down to 2 K. This contrasts with the resistivity behavior of pristine graphene which shows a small increase (around 10%) at temperatures in the range of mK⁴⁸. The increase in the peak resistivity is consistent with the confinement of quasiparticles, as discussed in the 2D VRH analysis above.

Gate-dependent resistance oscillations

The periodic magnetic potential in graphene is expected to generate secondary Dirac points in the band structure and lead to periodic features in the gate-dependent resistivity¹¹. Figure 3b shows the same 2 K data as in Fig. 3a but for a narrower range of V_g . A series of gate voltage dependent resistivity

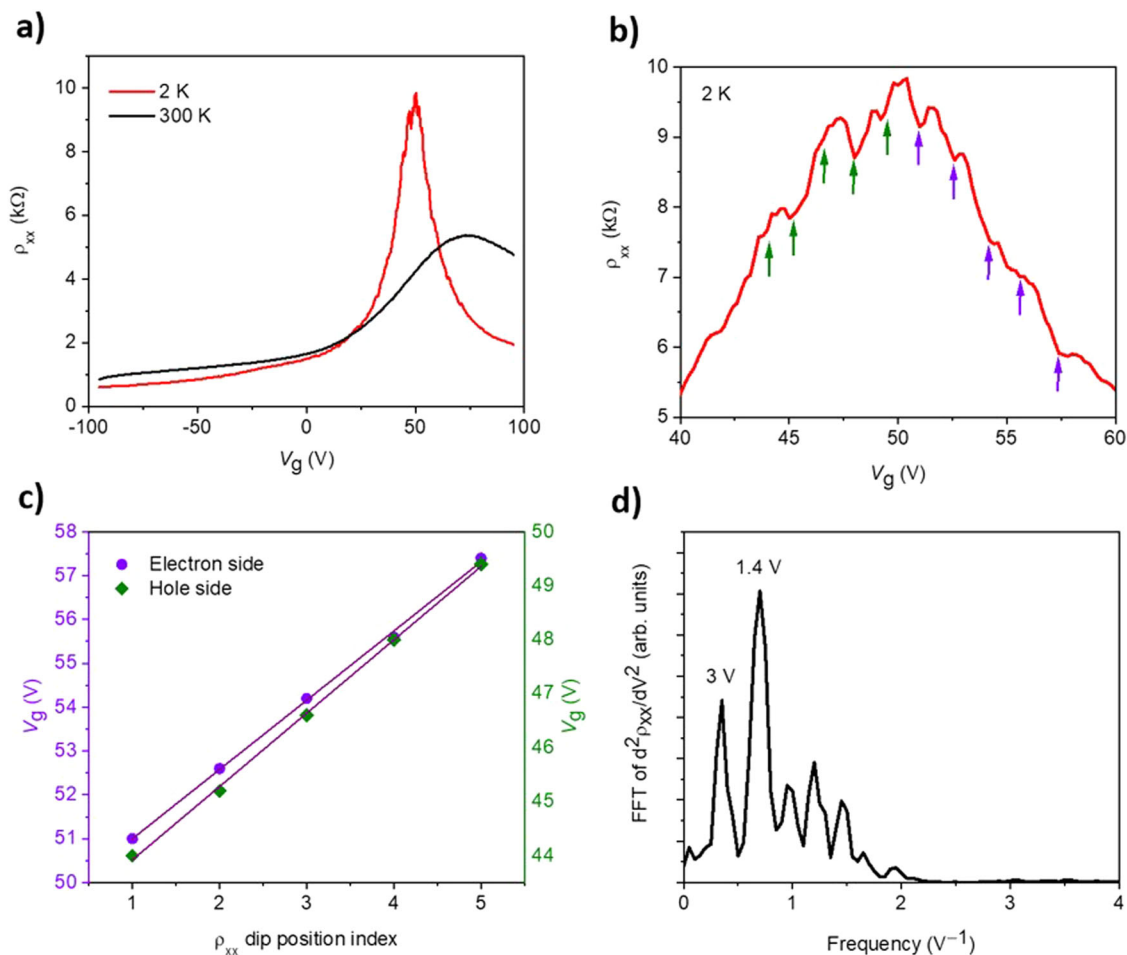


Fig. 3 | Gate voltage and temperature dependence of longitudinal resistivity (ρ_{xx}) of the graphene/Fe₃O₄ NS system. a Gate voltage dependence of ρ_{xx} at 300 and 2 K. Peak resistivity nearly doubles and the Dirac point (DP) shifts from 74 V to 50.2 V as the temperature is decreased to 2 K. **b** The same data shown in (a) at 2 K but between

40 and 60 V. Nearly equally spaced resistivity peaks are evident, as indicated by arrows. The resistivity dips for both the hole and electron sides occur in nearly equal spaced gate voltage values as shown in (c) and the spacing was determined to be 1.4 V by fast Fourier transform analyses as shown in (d).

dips are evident, as indicated by arrows. These resistivity dips, for both the electron and hole sides, are nearly equally spaced in V_g , as shown in Fig. 3c. The periodicity of the resistivity dips is $\Delta V_{\text{dip}} \sim 1.4$ V, determined by fast Fourier transform analyses of the second derivative of the resistivity as a function of gate voltage as shown in Fig. 3d. These dips only arise in the presence of the nanospheres and below T_B , indicating their origin in a magnetic superlattice. Here, we took the second derivative of the resistivity as a function of gate voltage data in order to remove the background Dirac peak to obtain the low frequency of the resistance peaks (see Supplementary Note 4 for the details of the FFT analysis). We note that the resistivity dips we observe are not due to local doping by charge impurities or the Fe₃O₄ NSs even though the device is globally p-doped (Dirac peak centered at $V_g = 50.2$ V). In our earlier work on graphene strain superlattices⁵, we demonstrated that charged impurities play a negligible role in superlattice effect in graphene unless the impurity density reaches an order of $n_i \sim 10^{13}$ cm⁻², whereas our graphene strain superlattice devices show an impurity density of $n_i \sim 7 \times 10^{12}$ cm⁻². Similarly, in this work, the mobility of the charge carriers where the resistivity steps occur is $\mu \sim 10^3$ cm² V⁻¹ s⁻¹ which gives $n_i \sim 10^{12}$ cm⁻². Moreover, the superlattice Dirac points in our device are sensitive to external magnetic fields, which are not expected to affect locally electrostatically doped regions in graphene, as we show below.

To further elucidate the origin of the resistivity dips, we study their behavior as a function of magnetic field. In particular, the magnetic field modifies the magnetic properties of the NS. At zero magnetic field and

2 K, the NS residing on the graphene are ferromagnetic with a net magnetization making a finite angle with respect to the in-plane direction. The imprinted magnetization is evident from the hysteresis loop shown in Fig. 1d and is consistent with the Stoner-Wohlfarth model describing magnetization rotation of single-domain non-interacting particles with random distribution of anisotropy axes⁵⁰. Rotating the magnetization orientation using an external magnetic field, as shown in the inset of Fig. 1d, should thus modify the magnetic properties of the NS, and enable a determination of their effects on the resistivity dips.

Figure 4a shows ρ_{xx} vs V_g under external magnetic fields of 3, 7, and 9 T, as well as 0 T data as a reference. The resistivity curves for each field are intentionally shifted vertically for clarity. The finite field data shows two distinct features compared to the 0 T data: (i) small resistivity steps, which are shown by red arrows on the 3 T curve as an example. The 7 T and 9 T data display similar peaks, and (ii) broad resistivity dips shown with black arrows and corresponding to Landau energy levels with filling factors of $\nu = 2$ and $\nu = 6$ where $\nu = \pm 4(|n| + 1/2)$ where $n = 0, 1, 2, \dots$ ⁵¹. The filling factor ν can be directly derived from the minima of the ρ_{xx} versus V_g curves. The Landau level features do not appear below 7 T. To better examine the smaller resistivity steps, Fig. 4b shows the same data presented in Fig. 4a but for a range between - 5 V and - 25 V for 0 T and 3 T, between - 20 V and - 35 V for 7 T, and between - 25 V and - 35 V for 9 T; the data is also normalized for better comparison and analysis. It is clear that the resistivity steps become more

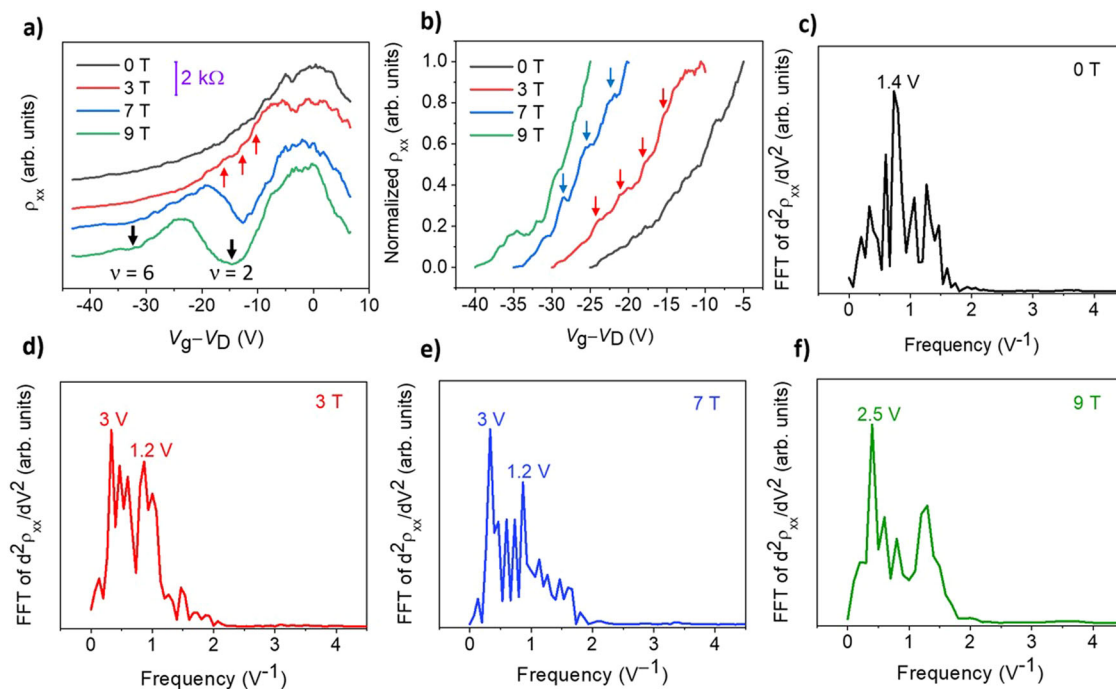


Fig. 4 | Longitudinal resistivity (ρ_{xx}) as a function of gate voltage (V_g) at different magnetic fields. **a Resistivity steps, shown with red arrows on the 3 T data as an example, are observed in a V_g range between -35 and 0 V for all magnetic field values. These steps are signatures of electronic structure modification in graphene by the magnetic superlattice. The plots are offset vertically for clarity. The resistivity peaks indicated with black arrows point to the Landau levels with filling factors of $\nu = 2$ and 6 . **b** Resistivity versus V_g . The data shown here is the normalized**

resistivity data shown in (a) for a range between -5 V and -35 V. The plot for 3 T is shifted horizontally by -5 V for clarity. The resistivity steps get sharper with increasing magnetic fields and their period increases as the field is increased up to 7 T, but decreases slightly at 9 T. The red and blue arrows show the prominent resistivity steps appearing at 3 and 7 T, respectively. **c-f** Fast Fourier transform of second derivative of ρ_{xx} with respect to V_g at 0 T, 3 T, 7 T, and 9 T respectively.

prominent as the field is increased up to 7 T and are then suppressed at 9 T where a filling factor of approximately 6 exists. This suppression is likely due to the interplay between magnetism imprinted in graphene and the external magnetic field. At high magnetic fields, in the quantum Hall regime, where the Landau levels are formed, the minibands formed due to the superlattice potentials can break up the Landau levels into sub-bands. However, the minibands, which are measured by depopulation with the gate voltage, will be sensitive to the magnetic field applied which changes the magnetic dipole orientation in the NSs and, thus the superlattice potentials. The periodicity of the steps is determined by fast Fourier transform (FFT) analyses, which yields 1.4 V for 0 T (shown in Figs. 4c) and 3 V, 3 V, and 2.5 V for 3, 7, and 9 T, respectively (shown in Fig. 4d-f). We note that the zero-field resistivity data shown in Figs. 3b and 4a were taken before and after thermal cycle i.e., after the device was cooled down to 2 K and warmed back to 300 K. Due to possible release in strain at the NS-graphene interface after thermal cycling, the FFT extracted from the data shown Fig. 3b is slightly different from the FFT presented in Fig. 4c. It is worth noting that the dominant zero-field FFT peak is 1.4 V in both FFT results. The 3 V peak is suppressed but not missing in Fig. 4c. Considering the evolution of the resistivity peaks with the magnetic field applied and slight change in the FFT results confirm the reliability of our data.

Self-consistent tight binding calculations

To further determine the relationship between the resistivity steps and the underlying superlattice of magnetic NS, we use a self-consistent tight-binding model of graphene⁵²⁻⁵⁴, with results shown in Fig. 5. In the tight-binding representation, we use 10 nm diameter NS with a center-to-center separation of 10 nm, which reflects the experimental device geometry. Given the proximity-induced magnetism in the graphene from the NS, we account for the magnetic interactions of the NS and the graphene via a mapping function that follows the pattern of the NS on the surface. The mapping function, $p(x,$

$y)$, is given a value of $0 \leq p(x, y) \leq M_{NS}$ depending on the real space separation of the NS and the surface of the graphene layer, where M_{NS} is the maximum magnetic moment of a NS and is oriented perpendicular to the surface of graphene. In Fig. 5a, we plot the calculated band structure corresponding to the arrangement of NS on the surface of graphene assuming a magnetic interaction peak of $M_{NS} = 0.2$ eV and in the absence of an additional external magnetic field (see the Supplementary Note 5 for details on how M_{NS} has been determined for the theoretical calculation). The plotted bands clearly reveal the presence of superlattice Dirac points in the energy spectrum as reflected in the bright points around the γ point and between the γ and μ as well as the γ and κ' points in the Brillouin zone. Close to the Dirac point of the graphene, we notice that the energy spectrum is gapped across momenta, leading to the possibility of the magnetic confinement of quasi-particles in the graphene layer. To calculate observables, we use a self-consistent approach within the tight-binding framework. Self-consistency is implemented using an iterative scheme between the Poisson equation, that provides the electrostatic contribution, and the Green's function, for the quantum mechanical properties, to obtain the ground state energy for a given set of system parameters.

Once the ground state is obtained, here defined as an error of ≤ 1 μ eV, then the density of states (DoS) is calculated using standard non-equilibrium Green's function techniques⁵⁵. In Fig. 5b, we plot the DoS for graphene without an external magnetic field where we find clear evidence of the magnetic imprint of the NS, most notably in the presence of a peak in the DoS at $E = 0$ eV. Furthermore, we observe peaks in the DoS that have similar spacings and energy scales as the experimental peaks (see the Supplementary Note 5 for details on how DoS has been converted to resistivity and on comparison between the experimental results and the theory).

In Fig. 5c, we apply an external magnetic field to the graphene layer of increasing magnitude from 3 T to 9 T, as was done in the experimental measurements, and plot the resulting normalized DoS. As is true with the $B = 0$ T, the application of the applied external magnetic field perpendicular

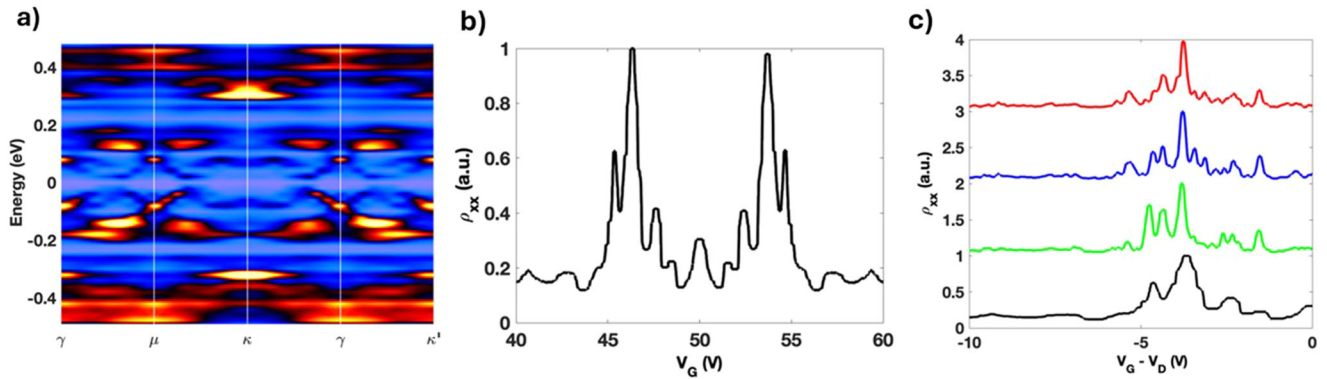


Fig. 5 | Self-consistent tight-binding model of graphene magnetic superlattice. **a** The band structure of graphene with a magnetic lattice of nanoparticles of separation 10 nm. We observe the existence of superlattice Dirac points at energies above $E = 0$, however, the spectrum close to the Dirac point at κ and κ' are now gapped from the magnetic interactions. **b** Inverse of the normalized DoS (which is proportional to ρ_{xx} under linear response theory) as a function of back gate voltage

(V_g) calculated in the presence of the magnetic nanospheres but with no external magnetic field. The Dirac point has been centered at $V_g = 50$ V and we observe the presence of the zero-energy peak in the DoS. **c** The density of states with the gate voltage of the Dirac point subtracted for applied magnetic fields of $B = 0$ T (black), 3 T (green), 7 T (blue), and 9 T (red), where the values have been normalized and offset for clarity.

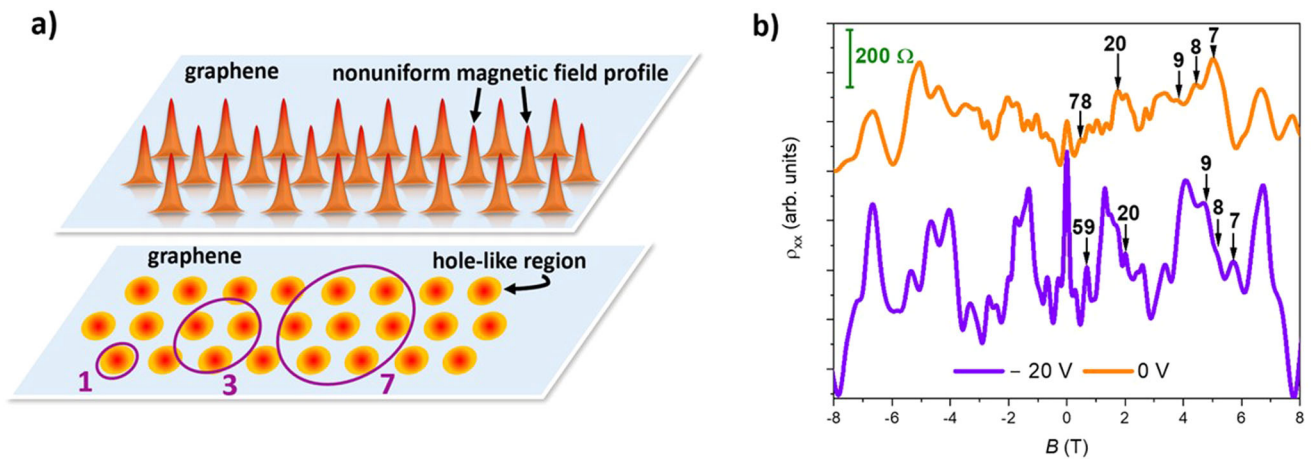


Fig. 6 | Magnetoresistance (MR) curves measured in an ‘antidot-like’ graphene superlattice at 2 K and gate voltages of -20 V and 0 V. **a** Upper panel: A schematic of the graphene magnetic superlattice structure consisting of circularly symmetric radially nonuniform magnetic field profile in a triangular lattice structure. Lower panel: graphene antidot-like superlattice structure consisting of impenetrable hole-

like energy barriers. **b** MR peaks corresponding to the diameter of the cyclotron orbit of the charge carriers commensurate with the center-to-center distance between the NS. Each peak corresponds to an integer number which states the number of NS enclosed by the cyclotron orbit. The resistivity peaks with missing numbers and arrows are described in Supplementary Fig. 7 in Supplementary Note 7.

to the graphene surface causes the electrons to undergo cyclotron orbits, which may be interrupted by the magnetic lattice which gaps the surface of the graphene.

According to the FFT analyses of the experimental data, the period of the resistivity peaks increases to 3 V at 3 T, and such a period is commensurate with the theoretical calculations. At 7 T, the period remains unchanged in both the theory and the experimental curves, with a corresponding decrease to 2.5 V at 9 T. The evolution of the resistivity steps, both period and intensity, is attributed to the competition between the cyclotron orbits induced by external magnetic field and the imprinted magnetism from the NS. From the experimental perspective, when magnetic fields of 3 T and 7 T are applied to the system, the magnetization vector of the NS rotates, and thus, the magnetic field profile of the NS changes. As the magnetization vector is aligned out of plane, the effect of the periodic magnetic potential becomes visible and sharper, and the period increases. This persists up to 7 T which is much larger than the saturation magnetization of the NS only and can be attributed to the canted surface spin structure interacting with graphene. At higher magnetic fields as high as 9 T, the external magnetic field wipes out the effects of the imprinted magnetism of the NS and the magnetic

field becomes almost uniform everywhere. This results in the weakening of the resistivity steps. Moreover, the emergence of the first two Landau levels possibly affects the steps, as well.

Quasi-periodic magnetoresistance oscillations

Finally, we turn our attention to magnetoresistance (MR) signatures of an NS-induced antidot array. The magnetic field profile on graphene under each NS is circularly symmetric and radially inhomogeneous i.e., $B = B(r)\hat{z}$ when finite external magnetic field is applied as shown in Fig. 6a upper panel. Such an inhomogeneous magnetic profile can suppress Klein tunneling of charge carriers in graphene¹⁶. Therefore, the transport in the graphene magnetic superlattice device can be considered as a graphene antidot system, similar to the case of lithographically patterned periodic holes in graphene^{56,57}, because of the presence of the impenetrable circular energy barriers as shown in Fig. 6a lower panel. The presence of hole-like energy barriers in the graphene magnetic superlattice device alters the cyclotron motion of the charge carriers. The orbits can be chaotic or circular depending on the magnitude of the external magnetic field as they are interrupted by the circular energy barriers. In graphene antidot systems⁵⁷, MR peaks emerge when the diameter of the cyclotron orbit $2R_c$ is

commensurate with the center-to-center distance λ between the antidots: $2R_c = \alpha\lambda$. Here, $R_c = \hbar k_F / eB$ where $k_F = \sqrt{\pi n}$ is the Fermi wave number and α is an integer $\alpha = 1, 2, 3, \dots$ corresponding to the number of antidots encircled by the cyclotron orbit. Figure 6a lower panel shows cyclotron orbits encircling 1, 3, and 7 antidot or circular energy barriers as an example. To investigate the validity of the ‘antidot’ hypothesis, we performed MR measurements at gate voltages -20 V ($n = 5 \times 10^{12} \text{ cm}^{-2}$) and 0 V ($n = 3.6 \times 10^{12} \text{ cm}^{-2}$), as shown in Fig. 6b. The MR data exhibit multiple peaks and oscillations as a function of gate voltage and magnetic field. The sharp peaks around 0 T (-0.3 to 0.3 T) for both the -20 V and 0 V data consistent with weak localization, i.e., interference of pairs of back scattered electrons with time reversal symmetry⁵⁸. Above 6 T, broad Shubnikov-de Haas oscillations appear. Between ± 0.3 T and ± 6 T, other MR peaks appear, that are reproducible and quasiperiodic, and are consistent with MR due to cyclotron orbits around antidots. Some of the MR peaks are indicated with arrows and integer numbers which correspond to the number of NS, or hole-like regions encircled by the cyclotron orbits. As an example, take the MR peak of the -20 V data indicated by 59. For $n = 5 \times 10^{12} \text{ cm}^{-2}$, $\alpha = 59$, $B = 0.681$ T, we obtain a superlattice periodicity to be $\lambda = 13$ nm. The MR peak of the 0 V shown with 7 corresponds to $B = 5$ T which is determined for $n = 3.6 \times 10^{12} \text{ cm}^{-2}$ and $\lambda = 12.6$ nm. The superlattice periodicity determined by the semi-classical $2R_c = \alpha\lambda$ equation is consistent with the periodicity determined by the TEM studies (Supplementary Fig. 1a) and SEM studies (Supplementary Fig. 3 inset 3). The quasiperiodic MR peaks we observe have been used to support our hypothesis of ‘magnetic confinement of the quasiparticles’. As the weak localization peak at 0 T diminishes, the peak corresponding to the largest cyclotron orbit appears. This orbit corresponds to the electrons encircling 59 NSs. Considering that the diameter of the NSs is 11 nm, then the length of this cyclotron orbit is around 100 nm. This value is close to the phase coherence length $L_\phi = 112$ nm at $V_g = -20$ V (see Supplementary Note 6 for the details of determining L_ϕ and the weak localization fitting in Supplementary Fig. 5 and the average domain size of the NS self-assemblies (~ 100 nm) in Supplementary Fig. 6). Thus, infer that the cut-off length for the cyclotron orbits is determined by the domain size of the nanospheres which also corresponds to the phase coherence length.

In summary, we demonstrate how a periodic magnetic lattice generated by Fe_3O_4 NS self-assemblies can imprint its magnetism in graphene and modify its band structure. The magnetic lattice on graphene leads to the formation of superlattice Dirac points in the electronic band structure. This is observed in transport measurements as gate-dependent resistance steps which can be tuned by an external magnetic field. Band structure calculations using a self-consistent tight binding model confirm the presence of superlattice Dirac points and provide a microscopic understanding of how the charge carriers are magnetically confined around the nanospheres. This carrier localization leads to anomalous quasi-periodic magnetoresistance oscillations. Further experiments are required to understand the effects of size and magnetic anisotropy of the NS on the generated superlattice, and the chemical and physical nature of the interface between the NS and graphene, and their role in proximity-induced ferromagnetism. For example, angle-resolved photoemission spectroscopy can be used to image the superlattice Dirac cones and gapped band structure near the κ and κ' points. Magnetic scanning gate microscopy can be used to image the magnetic domains induced in graphene. Our results elucidate the effects of a magnetic superlattice on graphene and demonstrate a technique for graphene band structure engineering that is scalable and field-tunable and can be extended to other two-dimensional van der Waals and topological materials.

Methods

Monolayer graphene, grown on $35 \mu\text{m}$ thick copper foil using chemical vapor deposition, purchased from ACS Material LLC, was transferred onto SiO_2 (300 nm)/Si substrates using standard wet transfer techniques. A 0.1 M aqueous solution of ammonium persulfate was used to etch the copper layer away. The graphene layer, supported by a $\sim 200 \text{ nm}$

thick layer of PMMA, was then scooped onto the substrate. After the sample was dried, the PMMA layer was removed by acetone. The transferred graphene was then etched into a Hall bar geometry using electron beam lithography, with 950 PMMA A4 (purchased from Kayaku Advanced Materials) acting as a positive resist, and oxygen plasma reactive ion etching. The Hall bar device described in this manuscript is of length $L = 6 \mu\text{m}$ and width $W = 1 \mu\text{m}$. A second e-beam lithography step, along with e-beam metal evaporation, was used to pattern Ti (5 nm)/Au (20 nm) electrodes onto the graphene Hall bar. A third e-beam lithography step was used to create a ‘window’ in the PMMA-resist layer, selectively at the location of the graphene device. After the iron oxide (Fe_3O_4) nanospheres (NS) were transferred onto the sample, this layer of PMMA was removed via acetone. Thus, the self-assembly of iron oxide NS covered only the graphene Hall bar device and not the entirety of the chip. Thermal annealing under forming gas at 300 C for 30 min was performed to remove the organic ligand shell around the NS on the graphene Hall bar device. The device was wire-bonded, and all transport measurements were performed inside a Quantum Design Physical Property Measurement System (Quantum Design PPMS Dynacool) which uses pulse tube refrigeration to cool down to a base temperature of 1.8 K and is equipped with a 9 T superconducting magnet in the out-of-plane direction. Measurements were performed via the lock-in technique in an AC current bias mode (100 nA , 14 Hz) using National Instruments SR830 lock-in amplifiers. The gate voltage was tuned using a Tektronix Keithley 2400 Source meter. The magnetic properties of the nanoparticles were characterized using SQUID magnetometry in a Quantum Design Magnetic Property Measurement System (MPMS3) with a standard quartz holder for in-plane magnetization measurements and a straw holder for out-of-plane measurements.

Data availability

The data used in this study are available upon reasonable request from the corresponding author O.T. (onurtosunn@gmail.com).

Code availability

The code used in this study are available upon reasonable request from the corresponding author M.G. (matthewg@illinois.edu).

Received: 13 September 2023; Accepted: 31 March 2024;

Published online: 11 April 2024

References

- Geim, A. K. & Novoselov, K. S. The rise of graphene. *Nat. Mater.* **6**, 183–191 (2007).
- Novoselov, K. S., Mishchenko, A., Carvalho, A. & Neto, A. H. C. 2D materials and van der Waals heterostructures. *Science* **353**, aac9439 (2016).
- Cao, Y. et al. Unconventional superconductivity in magic-angle graphene superlattices. *Nature* **556**, 43–50 (2018).
- Wei, P. et al. Strong interfacial exchange field in the graphene/EuS heterostructure. *Nat. Mater.* **15**, 711–716 (2016).
- Zhang, Y., Kim, Y., Gilbert, M. J. & Mason, N. Electronic transport in a two-dimensional superlattice engineered via self-assembled nanostructures. *npj 2D Mater. Appl.* **2**, 1–6 (2018).
- Zhang, Y., Kim, Y., Gilbert, M. J. & Mason, N. Magnetotransport in a strain superlattice of graphene. *Appl. Phys. Lett.* **115**, 143508 (2019).
- Ye, P. et al. Electrons in a periodic magnetic field induced by a regular array of micromagnets. *Phys. Rev. Lett.* **74**, 3013 (1995).
- Izawa, S. I., Katsumoto, S., Endo, A. & Iye, Y. Magnetoresistance oscillation in two-dimensional electron gas under spatially modulated vector potential. *J. Phys. Soc. Jpn.* **64**, 706–710 (1995).
- Overend, N. et al. Temperature dependence of large positive magnetoresistance in hybrid ferromagnetic/semiconductor devices. *Appl. Phys. Lett.* **72**, 1724–1726 (1998).

10. Brey, L. & Fertig, H. Emerging zero modes for graphene in a periodic potential. *Phys. Rev. Lett.* **103**, 046809 (2009).
11. Barbier, M., Vasilopoulos, P. & Peeters, F. Extra Dirac points in the energy spectrum for superlattices on single-layer graphene. *Phys. Rev. B* **81**, 075438 (2010).
12. Pham, C. H., Nguyen, H. C. & Nguyen, V. L. Massless Dirac fermions in a graphene superlattice: a T-matrix approach. *J. Phys. Condens. Matter* **22**, 425501 (2010).
13. Park, C.-H. et al. Anisotropic behaviours of massless Dirac fermions in graphene under periodic potentials. *Nat. Phys.* **4**, 213–217 (2008).
14. Li, Y. et al. Anisotropic band flattening in graphene with one-dimensional superlattices. *Nat. Nanotechnol.* **16**, 525–530 (2021).
15. Katsnelson, M., Novoselov, K. & Geim, A. Chiral tunnelling and the Klein paradox in graphene. *Nat. Phys.* **2**, 620–625 (2006).
16. De Martino, A., Dell’Anna, L. & Egger, R. Magnetic confinement of massless Dirac fermions in graphene. *Phys. Rev. Lett.* **98**, 066802 (2007).
17. Masir, M. R., Vasilopoulos, P., Matulis, A. & Peeters, F. Direction-dependent tunneling through nanostructured magnetic barriers in graphene. *Phys. Rev. B* **77**, 235443 (2008).
18. Le, V. Q., Pham, C. H. & Nguyen, V. L. Magnetic Kronig–Penney-type graphene superlattices: finite energy Dirac points with anisotropic velocity renormalization. *J. Phys. Condens. Matter* **24**, 345502 (2012).
19. Dell’Anna, L. & De Martino, A. Magnetic superlattice and finite-energy Dirac points in graphene. *Phys. Rev. B* **83**, 155449 (2011).
20. Cao, Y. et al. Superlattice-induced insulating states and valley-protected orbits in twisted bilayer graphene. *Phys. Rev. Lett.* **117**, 116804 (2016).
21. Regnault, N. & Bernevig, B. A. Fractional Chern insulator. *Phys. Rev. X* **1**, 021014 (2011).
22. Spanton, E. M. et al. Observation of fractional Chern insulators in a van der Waals heterostructure. *Science* **360**, 62–66 (2018).
23. Xie, Y. et al. Fractional Chern insulators in magic-angle twisted bilayer graphene. *Nature* **600**, 439–443 (2021).
24. Gong, C. & Zhang, X. Two-dimensional magnetic crystals and emergent heterostructure devices. *Science* **363**, eaav4450 (2019).
25. Huang, B. et al. Emergent phenomena and proximity effects in two-dimensional magnets and heterostructures. *Nat. Mater.* **19**, 1276–1289 (2020).
26. Kurebayashi, H., Garcia, J., Khan, S., Sinova, J. & Roche, S. Magnetism, symmetry and spin transport in van der Waals layered systems. *Nat. Rev. Phys.* **4**, 150–166 (2022).
27. Tenasini, G. et al. Band gap opening in bilayer graphene-CrCl₃/CrBr₃/CrI₃ van der Waals interfaces. *Nano Lett.* **22**, 6760–6766 (2022).
28. Jiang, S., Li, L., Wang, Z., Mak, K. & Shan, J. Controlling magnetism in 2D CrI₃ by electrostatic doping. *Nat. Nanotechnol.* **13**, 549–553 (2018).
29. Chan, K. T., Neaton, J. & Cohen, M. L. First-principles study of metal adatom adsorption on graphene. *Phys. Rev. B* **77**, 235430 (2008).
30. Giovannetti, G. et al. Doping graphene with metal contacts. *Phys. Rev. Lett.* **101**, 026803 (2008).
31. Uchoa, B., Kotov, V. N., Peres, N. & Neto, A. C. Localized magnetic states in graphene. *Phys. Rev. Lett.* **101**, 026805 (2008).
32. Krasheninnikov, A. et al. Embedding transition-metal atoms in graphene: structure, bonding, and magnetism. *Phys. Rev. Lett.* **102**, 126807 (2009).
33. Uchoa, B. & Neto, A. C. Superconducting states of pure and doped graphene. *Phys. Rev. Lett.* **98**, 146801 (2007).
34. Song, G., Ranjbar, M., Daughton, D. R. & Kiehl, R. A. Nanoparticle-induced anomalous hall effect in graphene. *Nano Lett.* **19**, 7112–7118 (2019).
35. Park, J. et al. Ultra-large-scale syntheses of monodisperse nanocrystals. *Nat. Mater.* **3**, 891–895 (2004).
36. Manohar, A. & Krishnamoorthi, C. Low Curie-transition temperature and superparamagnetic nature of Fe₃O₄ nanoparticles prepared by colloidal nanocrystal synthesis. *Mater. Chem. Phys.* **192**, 235–243 (2017).
37. Santoyo Salazar, J. et al. Magnetic iron oxide nanoparticles in 10–40 nm range: composition in terms of magnetite/maghemite ratio and effect on the magnetic properties. *Chem. Mater.* **23**, 1379–1386 (2011).
38. Majetich, S. & Sachan, M. Magnetostatic interactions in magnetic nanoparticle assemblies: energy, time and length scales. *J. Phys. D: Appl. Phys.* **39**, R407 (2006).
39. Tong, S., Quinto, C. A., Zhang, L., Mohindra, P. & Bao, G. Size-dependent heating of magnetic iron oxide nanoparticles. *ACS Nano* **11**, 6808–6816 (2017).
40. Zeng, H. et al. Magnetotransport of magnetite nanoparticle arrays. *Phys. Rev. B* **73**, 020402 (2006).
41. Gauding, E. A. et al. Deposition of wafer-scale single-component and binary nanocrystal superlattice thin films via dip-coating. *Adv. Mater.* **27**, 2846–2851 (2015).
42. Yamamoto, K., Hogg, C. R., Yamamuro, S., Hirayama, T. & Majetich, S. Dipolar ferromagnetic phase transition in Fe₃O₄ nanoparticle arrays observed by Lorentz microscopy and electron holography. *Appl. Phys. Lett.* **98**, 072509 (2011).
43. Hill, R. M. Variable-range hopping. *Phys. Status Solidi (a)* **34**, 601–613 (1976).
44. Wang, Y. et al. Electronic properties of nanodiamond decorated graphene. *ACS Nano* **6**, 1018–1025 (2012).
45. Zhang, H. et al. Large-scale mesoscopic transport in nanostructured graphene. *Phys. Rev. Lett.* **110**, 066805 (2013).
46. Pan, J. et al. Correlation hard gap in antidot graphene. *Phys. Rev. B* **103**, 235114 (2021).
47. Reijniers, J., Peeters, F. & Matulis, A. Electron scattering on circular symmetric magnetic profiles in a two-dimensional electron gas. *Phys. Rev. B* **64**, 245314 (2001).
48. Tan, Y.-W., Zhang, Y., Stormer, H. L. & Kim, P. Temperature dependent electron transport in graphene. *Eur. Phys. J. Spec. Top.* **148**, 15–18 (2007).
49. Wu, Q.-P., Liu, Z.-F., Chen, A.-X., Xiao, X.-B. & Miao, G.-X. Tunable Dirac points and high spin polarization in ferromagnetic-strain graphene superlattices. *Sci. Rep.* **7**, 1–10 (2017).
50. Stoner, E. C. & Wohlfarth, E. A mechanism of magnetic hysteresis in heterogeneous alloys. *Philos. Trans. R. Soc. Lond., Ser. A* **240**, 599–642 (1948).
51. Park, C.-H., Son, Y.-W., Yang, L., Cohen, M. L. & Louie, S. G. Landau levels and quantum Hall effect in graphene superlattices. *Phys. Rev. Lett.* **103**, 046808 (2009).
52. Basu, D., Gilbert, M. J., Register, L. F., Banerjee, S. K. & MacDonald, A. H. Effect of edge roughness on electronic transport in graphene nanoribbon channel metal-oxide-semiconductor field-effect transistors. *Appl. Phys. Lett.* **92**, 042114 (2008).
53. Gilbert, M. J. Finite-temperature pseudospin torque effect in graphene bilayers. *Phys. Rev. B* **82**, 165408 (2010).
54. Pedersen, T. G. & Pedersen, J. G. Self-consistent tight-binding model of B and N doping in graphene. *Phys. Rev. B* **87**, 155433 (2013).
55. Hirsbrunner, M. R. et al. A review of modeling interacting transient phenomena with non-equilibrium Green functions. *Rep. Prog. Phys.* **82**, 046001 (2019).
56. Jessen, B. S. et al. Lithographic band structure engineering of graphene. *Nat. Nanotechnol.* **14**, 340–346 (2019).
57. Sandner, A. et al. Ballistic transport in graphene antidot lattices. *Nano Lett.* **15**, 8402–8406 (2015).
58. Chen, Y.-F. et al. Magnetoresistance in single-layer graphene: weak localization and universal conductance fluctuation studies. *J. Phys. Condens. Matter* **22**, 205301 (2010).

Acknowledgements

This manuscript is based upon work supported by the Army Research Office, under Award No. W911-NF191-0346. In addition, P.S. acknowledges support from the NSF-MRSEC Award DMR-1720633. This work was carried out in part in the Materials Research Laboratory Central Research Facilities, University of Illinois, and used facilities supported by the NSF-MRSEC DMR-2309037.

Author contributions

O.T., M.G., Q.C., and N.M. conceived the experiment. O.T. designed and fabricated devices and carried out transport measurements. P.S. carried out the magnetization measurements. C.Q. synthesized and transferred the nanoparticle assemblies on the graphene device. M.G. performed the tight binding calculations. O.T., P.S., C.Q., M.G., Q.C., and N.M. analyzed the data and wrote the manuscript.

Competing interests

The authors declare no competing interests.

Additional information

Supplementary information The online version contains supplementary material available at

<https://doi.org/10.1038/s41699-024-00468-7>.

Correspondence and requests for materials should be addressed to Onur Tosun or Nadya Mason.

Reprints and permissions information is available at <http://www.nature.com/reprints>

Publisher's note Springer Nature remains neutral with regard to jurisdictional claims in published maps and institutional affiliations.

Open Access This article is licensed under a Creative Commons Attribution 4.0 International License, which permits use, sharing, adaptation, distribution and reproduction in any medium or format, as long as you give appropriate credit to the original author(s) and the source, provide a link to the Creative Commons licence, and indicate if changes were made. The images or other third party material in this article are included in the article's Creative Commons licence, unless indicated otherwise in a credit line to the material. If material is not included in the article's Creative Commons licence and your intended use is not permitted by statutory regulation or exceeds the permitted use, you will need to obtain permission directly from the copyright holder. To view a copy of this licence, visit <http://creativecommons.org/licenses/by/4.0/>.

© The Author(s) 2024